Journal of Thermal Analysis and Calorimetry (2022) 147:9353–9365
https://doi.org/10.1007/s10973-022-11236-4

Plasma-assisted preparation of nano-(ZrC, ZrO_2)@carbon composites from Zr-loaded sulfonated styrene–divinylbenzene copolymers

Alejandro Martiz[1,2] · Zoltán Károly[2] · László Trif[2] · Miklós Mohai[2] · Laura Bereczki[2] · Péter Németh[3] · Zsombor Molnár[4] · Alfréd Menyhárd[1] · Rajendra P. Pawar[5] · Sunil Tekale[6] · László Kótai[2,7]

Received: 6 November 2021 / Accepted: 18 January 2022 / Published online: 17 February 2022

Abstract

We have developed a simple method to prepare nano-($ZrC_{0.93}$, ZrO_2-polymorphs)@carbon composites with graphite/amorphous carbon content and adjustable Zr/C ratio based on using a multistep tube furnace and plasma-assisted heat treatment of zirconium-loaded sulfonated styrene–divinylbenzene (STY-DVB) copolymers. Pre-pyrolysis of zirconium-loaded sulfonated STY-DVB ion exchangers with 2 and 8 mass % DVB at temperatures between 1000 and 1400 °C for 2 h produced nano-ZrO_2@C intermediates with particle sizes of ~ 30–60 nm with no ZrC formation. Plasma processing of nano-ZrO_2@C resulted in nano-($ZrC_{0.93}$, ZrO_2)@C composites with 11% (under a He atmosphere) (C/Zr = 73) or 13% (under a H_2 atmosphere) (C/Zr = 58) $ZrC_{0.93}$ content. Three polymorphs of the zirconium dioxide (tetragonal, monoclinic and cubic, between 18 and 27 nm) were found in the products. The amounts of tetragonal and monoclinic ones are comparable to that of $ZrC_{0.93}$. The average particle size of $ZrC_{0.93}$ prepared in this way was found to be 21–23 nm. The BET surface area of the nano-($ZrC_{0.93}$, ZrO_2)@C(graphite) composites prepared in He and H_2 was over 250 and 300 m^2/g, respectively. We developed a reproducible and easy method to prepare nano-(ZrC, ZrO_2)@C products by setting the DVB content, sulfonation degree, Zr loading and the thermal treatment conditions, which have an influence on the ZrC and graphite/amorphous carbon content of nano-ZrO_2@C intermediates. The zirconium-loaded sulfonated styrene–divinylbenzene (STY-DVB) copolymers (2 and 8 mass% DVB) or their thermal decomposition was characterized with vibrational spectroscopy, thermal analysis and DSC or powder XRD, BET, XPS and HRTEM methods, respectively.

Keywords Zirconium carbide · Zirconium dioxide · Polymorphs · Sulfonation degree · Styrene–divinylbenzene copolymer · Thermal decomposition, evolved gas analysis · Nanocomposites

Introduction

Zirconium carbide–carbon (ZrC@C) composites have been considered strategic materials in emitters and coatings for nuclear reactor fuels due to their high melting point, good mechanical properties, small neutron absorption cross section, high sorption capacity and radiolytic stability toward radioactive isotopes [1–4]. Zirconium dioxide and its composites with carbon are widely used in various branches of science and industry, e.g., in pharmaceutical industry [5–7],

✉ László Kótai
kotai.laszlo@ttk.hu

1 Department of Physical Chemistry and Materials Science, Budapest University of Technology and Economics, Műegyetem rakpart 3, Budapest 1111, Hungary

2 Research Centre for Natural Sciences, Institute of Materials and Environmental Chemistry, Magyar Tudósok krt 2, Budapest 1111, Hungary

3 Institute for Geological and Geochemical Research, Research Centre for Astronomy and Earth Sciences, Eötvös Loránd Research Network, Budaörsi út 45, Budapest 1111, Hungary

4 Research Institute of Biomolecular and Chemical Engineering, Nanolab, University of Pannonia, Egyetem út 10, Veszprém 8200, Hungary

5 Shiv Chhatrapati College, N-3, CIDCO, Aurangabad, Maharashtra 431 003, India

6 Department of Chemistry, Deogiri College, Aurangabad, Maharashtra 431 005, India

7 Deuton-X Ltd, Selmeci u. 89, Érd, Pest 2030, Hungary

catalysis and nanotechnology [8, 9] and chemical and environmental engineering [10–13]. Synthesis of various polymorphs of ZrO_2 for various purposes is an intensively studied area of zirconium chemistry [14].

There are two main routes of methods to synthesize ZrC@C composites: (a) the solid-state reactions between elementary carbon and Zr, ZrH_2 or ZrO_2, [15, 16] and (b) the reactions of zirconium or its compounds with organic carbon sources. The zirconium source and carbon compounds may be Zr and methyl halides [17, 18]. Zirconium acetate or zirconium oxychloride can also be reacted with sucrose [19, 20]. Sacks et al. used zirconium n-propoxide/n-propanol (as a zirconia source) and phenolic resin or glycerol as a carbon source, [21], and Martiz et al. used a plasma-assisted synthesis route from analogous starting materials [22]. Scales et al. synthesized porous, mechanically stable bead-like ZrC@C composites via carbothermal reduction of polyacrylonitrile-$ZrCl_4$ composites [3] and quaternary ammonium salt group containing styrene–divinylbenzene copolymers loaded with anionic zirconium complexes [4].

Zirconium carbide ceramic materials formed in direct reactions of Zr or Zr compounds and carbon or carbon precursors, even in the case of the most reactive ZrH_2, always contains some carbon vacancy [16]. The reaction of carbon-deficient ZrC_x structures with the free carbon results in the formation of non-stoichiometric $Zr_{1-x}C$ (carbon-rich) materials and increases their sinterability [23].

The mixed composites have great new utilization possibilities—they combine the advantageous effects of nano-ZrC and nano-ZrO_2 on a carbon matrix, e.g., the conductivity of ZrO_xC_y composites in the molten state leads to emerging new electrolytic technologies to prepare zirconium.

Earlier we developed a simple way to prepare bead-shaped stable carbon composites containing nanosized metal oxides from metal-ion-loaded sulfonated or iminodiacetate-functionalized styrene–divinylbenzene (STY-DVB) copolymers [24–26]. Scales et al. prepared ZrC from quaternary ammonium salt-functionalized anion exchangers loaded with anionic Zr-complexes [3]. These results prompted us to develop the preparation of nano-ZrO_2@C intermediates from Zr-loaded sulfonated STY-DVB copolymers so that we could study their direct transformation in RF thermal plasma into nano-ZrC@C materials.

We tested zirconium loading onto the sulfonated STY-DVB resins from aqueous zirconyl salt (chloride, sulfate and nitrate) solutions, to decide which was optimal. The degree of sulfonation and Zr loading can control the Zr/carbon ratio, whereas the DVB content has an influence on the mechanical properties of the resulting composites. The sulfonated polymer serves as a carbon source, solidification agent and ensures the homogeneous distribution of zirconium in the Zr-compound(s)@C composites produced in a simple hot N_2 tube-furnace pyrolysis process.

The labels of the prepared materials are generated as X-DVB-Zr- compound-T-t, where X stands for the DVB content in the initial sample, T corresponds to the temperature of pyrolysis (1000, 1200, 1400 °C), whereas t represents reaction time (2 or 8 h). The labels of the prepared samples are summarized in Table 1.

In this paper, we present the preparation and properties of nano-ZrO_2@C and nano-(ZrC, ZrO_2)@C composites prepared with a tube furnace and by subsequent RF thermal plasma treatment of Zr-loaded sulfonated STY-DVB resins. Also discussed in detail are the characterization of initial X-DVB and X-DVB-Zr polymers, including determining the sulfonation degree and the distribution of sulfonic acid groups on STY and DVB rings, and the influence on zirconium loading of anions in the zirconyl salts used.

Experimental

Preparation of samples

The sulfonated 2-DVB and 8-DVB resins (Varion KS-2 and KS-8) were soaked in water for 24 h, and the swelled beads were filled into a 20-cm-long column. Zr loading was performed with the use of a zirconyl chloride solution containing 0.5 mass % Zr, in 3 M HCl until reaching the maximum possible loading with zirconium was reached. The 2-DVB-Zr and 8-DVB-Zr samples swelled in water formed during Zr loading were conditioned for 3 h at 90 °C and 2 h at 110 °C in air at atmospheric pressure in a programmable furnace, with a heating rate of 10 °C min^{-1}. The beads were placed into a porcelain crucible and left to cool in a desiccator filled with CaO.

Table 1 Labels for samples used or prepared

Label	Description of sample
X-DVB	Sulfonated STY-DVB copolymers containing X = 2 or 8 mass % DVB
X-DVB-Zr	Zirconium-loaded samples of sulfonated STY-DVB copolymers containing X = 2 or 8 mass % DVB
X-DVB-ZrO_2-T-t	Samples containing ZrO_2 prepared from Zr-loaded sulfonated STY-DVB copolymers containing 2 or 8 mass % DVB, at the given T temperature and t carbonization time
8-DVB-ZrC	Plasma-treated samples containing ZrC from the 8-DVB-ZrO_2-1000–2 sample

Carbonization experiments

The resins were subsequently reduced in size in a planetary ball mill (225 rpm, 30 min) to under 63 µm. In each case, 1.6 g of samples were placed into quartz boats, and carbonization (pyrolysis) was performed in an alumina tubular furnace under Ar atmosphere. Three different temperatures (1000, 1200, 1400 °C) and two different times (2 and 8 h) were used. The heating rate and gas flow were constant at 15 °C min^{-1} and 1.5 $L{\cdot}min^{-1}$, respectively, for all the experiments.

RF plasma processing

Due to the high amount of water contained in the resins and the short residence time of the particles in RF plasma, the 2-DVB-Zr and 8-DVB-Zr samples could not be sufficiently carbonized directly. Therefore, a ZrO_2@C sample prepared by pyrolysis at 1000 °C for 2 hours[1] was exposed to in-flight thermal plasma processing in an inert (He) and a reducing (H_2) atmosphere. The experimental setup consisted of a reactor chamber with a radio-frequency inductively coupled plasma torch (PL-35, TEKNA Ltd, Canada) mounted on the top, an RF generator (LEPEL, USA) with a maximum power of 30 kW at 4–5 MHz, a cyclone, a filter unit and a vacuum pump.

The experimental system was presented in detail in [27, 28]. The solid samples were delivered into the plasma via a powder feeder (Praxair) with helium as carrier gas, with a flow rate of 5 $L{\cdot}min^{-1}$. The feeding probe was placed coaxially into the middle of the induction coil. The feeding rate of the powder was 3 $g{\cdot}min^{-1}$. The plasma and sheath gas were mixtures of argon and helium with a flow rate of 11 $L{\cdot}min^{-1}$ Ar and 6 $L{\cdot}min^{-1}$ He for the plasma gas as well as 35 $L{\cdot}min^{-1}$ Ar and 5 $L{\cdot}min^{-1}$ He for the sheath gas. The same test was repeated with hydrogen added into the sheath gas with a flow rate of 5 $L{\cdot}min^{-1}$.

The samples prepared from resins with 2 mass % DVB content were not as stable mechanically as samples prepared from resins containing 8 mass % DVB. The size of nano-ZrO_2 (~60 nm) particles prepared at 1000, 1200 or 1400 °C for 2 h did not change considerably with increasing temperature. The sample prepared at 1400 °C in 8 h contained smaller (~20 nm) and probably more reactive ZrO_2 particles than the samples prepared at 1000 or 1200 °C, but this sample contained an unknown cubic phase (a = 0.76 nm); therefore, we did not consider it further for the preparation of ZrC@C composites.

Table E1 shows the most important operating conditions for the particular tests. The tests were performed under a pressure of 70 kPa, and the power was set to 25 kW.

Elemental analysis

CHS analysis: Samples were dried in a Heraeus vacuum oven (Thermo Electron, Germany) in glass vials at 140 °C for 19 h, filled with nitrogen, tightly capped and sealed with plastic film to maintain dryness until further analysis with a Carlo Erba 1106 instrument.

Specific surface area measurements

We calculated the specific surface area (SSA) using the Brunauer–Emmett–Teller (BET) equation based on nitrogen adsorption measurements at 77 K (Autosorb 1C, Quantachrome, seven-point isotherm). Desorption of the samples was performed under vacuum for 24 h at 100 °C. The average size of the particles was calculated with the equation: SSA [$m^2\ g^{-1}$] = 6/ρd, where ρ is absolute particle density [$g\ cm^{-3}$] and d is particle diameter [µm], assuming spherical particles.

Transmission Electron Microscopy

Transmission electron microscopy (TEM) was carried out with a 200 keV Talos Thermo Scientific transmission electron microscope. Grains were crushed in ethanol and deposited onto copper grids covered by Lacey carbon. We obtained bright-field TEM (BFTEM), high-resolution TEM (HRTEM) and high-angle annular dark-field (HAADF) scanning TEM images as well as selected-area electron diffraction (SAED) patterns. In TEM mode, the current was ~ 600 pA and the SAED patterns were obtained with a camera length of 520 mm. We performed elemental mapping in STEM mode in order to study the chemical composition and heterogeneity of the grains. In STEM mode, the current was ~ 200 pA. Beam convergence was 10.5 mrad, camera length was 125 mm, and dwell time was 10 µs. We used a "Super-X" detector system with four silicon drift detectors built into the microscope column. Fast Fourier transforms (FFTs) were calculated from the HRTEM images with Gatan Digital Micrograph 3.6.1 software. The details of TEM spectroscopy are given in [29].

Thermal studies

We performed simultaneous thermogravimetric analysis (TGA), differential scanning calorimetry (DSC) and mass spectrometric evolved gas analysis (MS-EGA) using a SETARAM Labsys Evo and a Pfeiffer Vacuum OmniStar instrument under high-purity helium (6.0) with a heating rate of 10 °C min^{-1} from room temperature to 1600 °C. The details of thermal measurements are given in [30, 31].

Scanning Electron Microscopy

We used a scanning electron microscope (SEM, Zeiss type DSM 982 GEMINI with a field emission tungsten cathode) in establishing the morphology of the resins. Prior to the analysis, all samples were coated with an Au layer of 2–3 nm thickness. Backscattered electron images of ground and polished samples were acquired; the accelerating voltage was 10 kV.

Powder X-ray diffraction

Powder XRD patterns were acquired with a Philips Bragg–Brentano parafocusing goniometer with the use of Cu weighted Kα radiation 1.5406/1.5444 Å in the range of 4–70º 2θ, a step size of 0.02º and an interval time of 1 s. Due to problems of determining the background, no goodness-of-fit parameters are given. The unit cell dimensions of the phases in all the patterns are well determined. The mass% of each phase should be considered an estimate rather than an accurate value. The details of the measurements are given in [31].

Vibrational spectroscopy

A Bruker Alpha FT-IR (Bruker, Ettingen, Germany) instrument and a Biorad-Digilab FTS-30-FIR far-IR instrument with a Smart iTR (attenuated total reflectance) accessory were used to collect the analytical and far-IR spectra, respectively. Spectra were made from 16 scans and acquired with a resolution of 4 cm^{-1} [32–34].

For Raman spectroscopy, a Horiba Jobin–Yvon LabRAM-type micro-spectrometer was used with an external laser source of 532 nm Nd-YAG. The laser beam was focused on an objective of 20X (numerical aperture = 0.4). A confocal hole of 1000 µm was used in the confocal system, and a grating monochromator of 1800 mm^{-1} was used for light dispersion. The detected wavenumber was scanned with a resolution of 3 cm^{-1} with an accumulation time of 10 s er point for a spectral range of 100–4000 cm^{-1}.

X-ray photoelectron spectroscopy

X-ray photoelectron spectra of the RF-plasma-treated samples were recorded with a Kratos XSAM 800 instrument (fixed analyzer transmission mode, 40 eV pass energy, Mg $K_{\alpha 1,2}$ (1253.6 eV) excitation, $< 1 \cdot 10^{-7}$ Pa analysis chamber pressure). Survey spectra were recorded for both samples in the 100–1300 eV kinetic energy range. High-resolution spectra of the characteristic photoelectron lines of the Zr, O, S and C were recorded with 0.1 eV steps and a dwell time of 1 s. Quantitative analysis (after removal of the Shirley-type background) was performed with the XPS MultiQuant program with experimentally determined photoionization cross-section data [35] and asymmetry parameters [36]

Results and discussion

Preparation and properties of Zr-loaded ion-exchangers (2-DVB-Zr and 8-DVB-Zr)

Two styrene–divinylbenzene copolymer-based sulfonated ion-exchangers with 2 and 8 mass % divinylbenzene content (2-DVB and 8-DVB) were loaded with zirconyl chloride ($ZrOCl_2.8H_2O$) in a 3 M HCl solution. With the elemental analysis data of 2-DVB and 8-DVB resins (CHS analysis, ESI Table 2) and the zirconium content of the eluate formed

Table 2 ZrO_2 and ZrC content of composites

Sample	Carbon content/mass%		ZrO_2 content and size /mass%, nm			ZrC content and size/mass%, nm
	Graphite	Amorphous carbon	Tetragonal	Monoclinic	Cubic	
2-DVB-ZrO_2-1000–2	49	~15	11 (62)	25 (34)	–	–*
2-DVB-ZrO_2-1200–2	44	~28	14 (61)	14 (31)	–	–*
2-DVB-ZrO_2 – 1400–2	37	~43	8 (44)	12 (32)	–	–
2-DVB-ZrO_2 – 1400–8	20	~62	7 (32)	11 (32)	–	–
8-DVB-ZrO_2-1000–2	29	> 61	< 5 (62)	5 (70)	–	–
8-DVB-ZrO_2 – 1200–2	23	> 65	< 5 (61)	7 (71)	–	–
8-DVB-ZrO_2-1400–2	27	> 63	< 5 (58)	5 (67)	–	–
8-DVB-ZrO_2-1400–8	17	> 73	< 5 (20)	< 5 (27)	–	–**
8-DVB-ZrC-1000–2 (post-RF, Ar-He)	> 55	–	16 (20)	13 (27)	< 5 (27)	11 (23)
8-DVB-ZrC-1000–2 (post-RF, Ar-H_2)	> 55	–	17 (18)	10 (27)**	< 5 (22)	13 (21)

*Unidentified phases containing Zr were also observed

**Zr_3C_2 ($ZrC_{0.67}$) was also detected by XRD in a small amount in the sample made in the H_2 atmosphere

during Zr loading, and the amounts of resin and zirconyl salt used, the Zr/sulfonic acid ratio (loading rate), water content and the Zr/C ratio in the starting X-DVB-Zr samples can be calculated in the following way:

The DVB content in the samples determines the distribution of carbon content between the aromatic rings and aliphatic parts (-CH-CH_2- groups). With the analyzed carbon content, the number of styrene and DVB units in a weighted amount of sample can be determined.

The carbon content and DVB/STY ratio determine the number of hydrogen atoms that belong to the polymer chain (5 hydrogen atoms on every styrene ring, 4 hydrogen atoms on DVB rings and 3 or 6 hydrogen atoms belong to the aliphatic parts of the unsulfonated styrene and DVB rings, respectively).

The number of these hydrogen atoms does not change on sulfonation because formally only an SO_3 group is inserted into a C-H aromatic bond. All the other hydrogen content determined by the analysis must belong to the swelling water in the resin samples.

The sulfur is exclusively present in the form of -SO_3H groups. Thus, the sulfur content allows the calculation of the amount of sulfonic acid amount in the sample directly. In other words, the average sulfonation degree of the rings located in the cross-linked resin network can be calculated from the ratio of S/C and the ratio of the STY and DVB rings. These values were found to be 1.69 and 1.63 for the sulfonated styrene/DVB samples containing 2 and 8 mass % DVB, respectively.

With the amount of sulfonic acid groups and the bound zirconium content (it was determined indirectly from the zirconium content of the eluate [37]), the loading rate (Zr/SO_3H group), the Zr/C ratio of X-DVB-Zr samples can be easily calculated. The latter value is of paramount importance in predicting the forming of ZrC.

The Zr/C atomic ratios calculated from the measurements were found to be 0.452 and 0.329 for the 2-DVB-Zr and 8-DVB-Zr samples, respectively. In principle, if the carbon loss during carbonization (degradation into volatile organic materials or CO/CO_2) is less than 58 mass % for 2-DVB-Zr samples or 66% for 8-DVB-Zr samples, then the residual carbon content in the solid phase is larger than is required to form stoichiometric ZrC. Depending on the amount of volatile carbon compounds (it depends on pressure, temperature, time and heating method) and the carbon loss during pyrolysis, the residual Zr/C ratio in nano-ZrO_2@C and nano-ZrC@C composites can be increased and only ZrC products with a carbon vacancy ($ZrC_{0.63-0.98}$ [23]) may be created.

The anion of the zirconium salt used during zirconium loading onto the sulfonated polymers has special importance. As is well-known, the zirconium (IV) ions hydrolyze and polymerize in their aqueous solutions, even under highly acidic conditions. [38] The exclusive form of zirconium(IV) in solutions above pH > 0 is generally a zirconyl ion (ZrO^{2+}), but the counter ion has remarkable effect on the nature of species containing Zr. Zirconyl nitrate ($ZrO(NO_3)2.5H_2O$), in the solid state, consists of $H_2[ZrO(NO_3)_4].H_2O$, which dissociates in its aqueous solutions with the formation of $ZrO(OH)NO_3$ [39] and turns into a non-ionic species. According to this, only 2 mass % of the initial zirconyl nitrate content was adsorbed with sulfonated cationic (Amberlite IR 100) ion exchangers [39].

Zirconium sulfate also strongly hydrolyzes in aqueous solutions, with the formation of basic zirconium sulfates, including zirconyl sulfate. The bond between sulfate ion and zirconium is strong. Since the affinity of zirconium to sulfate is higher than to water, this interaction remains stable in aqueous solutions as well. During the electrolysis of aqueous $Zr(SO_4)_2$ solutions, hydrogen evolution was observed on the cathode, and the species in the solution containing Zr was assigned as $H_2[ZrO(SO_4)_2.3H_2O]$ [39, 40]. This complex contains the zirconium in an anionic species, and it is not supposed to bind onto cation exchangers.

Zirconyl chloride ($ZrOCl_2.8H_2O$) exists in the solid state as a tetramer, $[Zr_4(OH)_8(H_2O)_{16}]Cl_8$ [38], and the zirconyl ion is the dominant form in aqueous solutions because the Zr^{4+} ion forms only in 12 M HCl solutions and with very low (0.0001 M) zirconium concentration [38]. We used a 0.055 M $ZrOCl_2.8H_2O$ solution in 3 M aq. HCl. Thus, the solution surely contained ZrO^{2+} and not Zr^{4+} ions. Based on the above-mentioned considerations, we selected the zirconyl chloride solution containing cationic species to use in zirconium loading experiments of the sulfonated DVB-STY resins. The Zr loading rate (Zr/SO_3H) on SO_3H functional groups was found to be 0.567 and 0.431 in the 2-DVB-Zr and 8-DVB-Zr samples, respectively. It suggests that no polymeric Zr cation ($(Zr_4(H_2O)_{16}(OH)_8{}^{8+}$) is loaded, but a simple zirconyl ion is the active cationic component in our X-DVB-Zr samples. This means that there are no observed intensive IR bands of the $[Zr_4O_4(OH)_8]^{8+}$cation [38] in the spectra of the Zr-loaded resins. The non-compensated charges of ZrO^{2+} ions are neutralized with neighboring "free" sulfonate and OH groups. We could not reach a saturation degree higher than ~ 80% even with an elongated sorption time on a dynamic column. It may be attributed to the differences between the steric hindrances of p- and o-positions of sulfonic acid groups on the STY and DVB rings, and probably only the easily available p-position sulfonic acid groups can bound zirconyl ions, whereas the sulfonic acid groups in sterically unfavorable o-positions cannot do that.

Spectroscopic characterization of X-DVB and X-DVB-Zr samples (X = 2 and 8)

IR spectroscopic characterization of X-DVB samples

The IR spectra of 2-DVB and 8-DVB resins showed the typical C-H and C–C/aromatic ring vibrational modes of the polystyrene-divinylbenzene copolymers [41, 42] and the typical normal modes of aromatic sulfonic acids [42] as well. The evaluation of the spectra is a serious challenge due to strong overlaps of polystyrene network and sulfonic acid modes. The most important peaks around 667, 1007, 1036, 1126 and 1175 cm^{-1} agree well with the reference values [41–49] given for sulfonated polystyrene and polystyrene-DVB samples. The peaks at 1007 cm^{-1} are assigned to the in-plane bending vibration of the benzene ring but may contain the Zr = O vibrational modes as well. [45] The band that appears at 1126 cm^{-1} is a combined band, it contains the in-plane skeleton vibration of the benzene ring in the mono-sulfonated polystyrene rings (as a sign of di-substitution), but the mode of ν_s(S–O) also appears in this band system confirmed by its shift to 1122 cm^{-1} when it forms a salt with zirconium(IV) (Table E3, ESI Figure E1).

The peaks at 669 and 673 cm^{-1} represent aromatic CH out-of-plane bending (deformation) vibrations, whereas the absence of peaks at around 699 and 759 cm^{-1} confirms complete sulfonation of all the styrene rings at least once. There are no peaks at 1680 cm^{-1} associated with the non-polymerized vinyl groups of cross-linkers. Thus, there are no unreacted pendant vinyl groups. A strong peak at 833 cm^{-1} together with no peak at 775 cm^{-1} indicates that the substitution on the styrene ring is mainly in the para position [46].

Although the reactivity of the DVB ring toward sulfonation is higher than that of the styrene ring due to the inductive effect of the two alkyl groups, no tri-sulfonated derivatives can be formed because of the low reactivity of the di-sulfonated species toward further sulfonation under the conditions used in ion-exchanger preparation (sulfonation with 96% sulfuric acid).

Thus, the 2-DVB and 8-DVB resins contain only mono- and di-sulfonated aromatic rings (STY and DVB). The first sulfonic acids are built into para- and ortho-positions of styrene and DVB rings, respectively. The favored ring positions for incorporation of the second sulfonic acid group are expected to be the ortho-positions of both rings due to ortho-induction of alkyl and m-induction of sulfonic acid groups of the mono-sulfonated derivatives. The sulfonation pathway is illustrated in Fig. 1. The average sulfonation degree of rings in 2-DVB and 8-DVB was found to be 1.63 and 1.69, respectively.

Vibrational spectroscopic characterization of Zr-loaded samples

A free sulfonate ion has a tetrahedral structure with pyramidal distortion (C3V local symmetry) with doubly degenerate antisymmetric stretching vibrations of S–O bonds in the sulfonate groups. The coordination of zirconyl ion to sulfonate groups may induce a change in local symmetry, depending on the coordination mode. A possible symmetric tridentate coordination mode (κ^1O, κ^1O^j, κ^1O^{jj} -SO_3-Zr(=O) does not change the original C_3v symmetry, whereas upon mono- or chelate-forming bidentate coordination of a zirconium ion, the C_3v symmetry of the -SO_3 – anions is distorted and becomes Cs symmetry. It results in the appearance of two vibrational bands of $\nu_{as}(SO_3)$ (Table E3).

In the experimental IR spectra of the X-DVB-Zr sample, we assigned the doubly degenerated ν_{as} mode as a band and as a shoulder at room temperature. It excludes the presence of the symmetric (C_{3v}) tridentate coordination mode of zirconium to the sulfonate groups and confirms the presence of a strong cation–anion interaction with a mono- or a bidentate coordination mode (Fig. 2) [42, 46].

The IR spectra of zirconyl salts containing mono- or bidentate coordinated sulfonate groups should be considerably different, but other factors, e.g., the contribution of ν (C-S) vibrational modes to ν (S–O) modes can make their assignation unambiguous. Nonetheless, DFT calculations on model compounds of sulfonated STY polymers with mono- and bidentate sulfonate groups showed that the bidentate sulfonate coordination mode always gave larger splitting of ν_{as}(S–O) bands than monodentate coordination modes. The experimentally found ~ 65 cm^{-1} splittings of ν_{as}(S–O) bands (decomposition of E degeneration) in the IR spectra of 2-DVB-Zr and 8-DVB-Zr suggest bidentate coordination modes of sulfonate groups to the zirconium in both samples. The coordination sphere of zirconium may contain hydroxyl ions (κ^1O, κ^1O^j -O-$SO_2Zr(OH)_2^+$ or water (κ^1O, κ^1O^j—$OSO_2Zr(O)(OH_2)^+$). The surplus + 1 charge can be compensated by the neighboring uncoordinated sulfonate, hydroxyl or hydrogen carbonate (due to the carbon dioxide from the air) ions. The evolution of CO_2 was detected by MS (Fig. 3, m/z = 44) on heating our wet samples to around 100 °C; therefore, we tried to detect the presence of the HCO_3^- ion precursor. Unfortunately, the position of the only intense stretching mode (ν_{as} (C-O)) and all the deformation modes in the IR spectra strongly coincide with bands of polymer network or water (ESI Table E1, Figures E2 and E3). The most intensive expected IR band of the hydrogen carbonate ion (ν_{as}(C-O)) is covered by other bands of the X-DVB samples. The intensity of ν_s(C-O) mode is very low in the IR spectra, but the highest in the Raman spectra of hydrogen carbonates. Thus, we tried to compare the Raman spectra of wet (we assumed the samples contained HCO_3^- ions) and

dry (we assumed they contained no HCO_3^- due to thermal decomposition during drying at 105 °C for 2 h) X-DVB-Zr samples (ESI Figures E2 and E3) to detect differences between the spectra. Unfortunately, the excitation laser of Raman spectroscopy causes local heating and decomposition of the carbonate species so the Raman spectra of the wet and dry samples were identical (ESI Figures E3). Thus, we cannot assign hydrogen carbonate as a CO_2 source. However, in the IR spectra, there were shoulders in the wet samples around 1200 cm^{-1}, which disappeared in the dry sample—this may be assigned to chemisorbed CO_2 bound as bidentate carbonate ions [50, 51]. We have no more information about the thermal stability of carbonates bidentately bound to zirconium, so the origin of CO_2 signals in the MS (Fig. 3) is left unexplained.

Thermal decomposition of X-DVB-Zr compounds

The analogs of styrene-DVB copolymers decompose on heating with the formation of solid carbonaceous materials and liquid/gaseous hydrocarbons [51–53]. The hardness and ratio of the solid carbon/liquid/gaseous decomposition materials depend on the DVB content. The increasing DVB content will increase the hardness and carbon content of the composite [24, 27, 52–54].

As metals are loaded into sulfonic acid groups, decomposition becomes more controlled, more solid product is formed, and the sulfonate groups are converted into gaseous SO_2 or, in the case of sulfidofilic metals, incorporate into solid sulfides [24, 25]. Zirconium does not belong to sulfidofilic elements. Therefore, the expected (and found) decomposition product (intermediate) is the oxide (ZrO_2), while carbide formation can be expected only at high temperatures [26] with reduction of Zr-oxide phases in the carbon-rich environment.

Thermal decomposition of 2-DVB-Zr and 8-DVB-Zr samples started analogously, namely with losing the swelling water from the pores of the hydrophilic polymer network phase around ~ 100 °C (ESI Figure E4a, g). No degradation of the organic part was observed in this temperature range. However, carbon dioxide formation was detected by TG-MS (m/z = 44, Fig. 3), which suggests that not only hydroxide ions but also hydrogen carbonate or carbonate ions may neutralize the charges of the zirconium cation.

The TG-MS curves for the main decomposition fragments (e.g., m/z = 64 and 48, SO_2^+ and SO^+, respectively) belonging to each decomposition step of 2-DVB-Zr and 8-DVB-Zr samples can be seen in Table E4 and ESI Figure E4 (c, i). The evolution of sulfur as SO_2 below the temperatures of ZrO_2 (or ZrC) formation show that the sulfur (sulfonic acid) content of the starting polymer does not directly affect ZrO_2 (ZrC) formation, and the sulfonate content plays a role only in adjusting the Zr/C ratio. Due to the appearance of organic fragments up to 800 °C (ESI Figure E5), the ZrO_2@C samples were prepared above this temperature (1000, 1200, and 1400 °C) with isothermal heating under N_2 in a tube furnace.

The shape of m/z = 64 and 48 (SO_2^+ and SO^+, respectively) curves (ESI Figure E4 (c, i)) is different for 2-DVB-Zr and 8-DVB-Zr. Sulfur dioxide evolution appears at a much lower temperature (289 and 410 °C) in the decomposition of 8-DVB-Zr than in that of 2-DVB-Zr (~ 400 and 490 °C). The coinciding decomposition peak temperatures of m/z = 64 (SO_2) and m/z = 76, 77 ($C_6H_4^+$ and $C_6H_5^+$) fragments show that these are formed in the same decomposition process, namely in the cleavage of aromatic rings with the formation of SO_2, water and organic fragments. No styrene but phenyl fragment formation was observed at 300 °C (ESI Fig. 5f, l) (there is no depolymerization at this temperature) in the case of 8-DVB-Zr (Fig. 5d,j). Styrene appears as a decomposition product, however, at 440 °C for both X-DVB-Zr samples (Fig. 5f,l). These results suggest that cross-linking has a great influence on the decomposition mechanism of the polymer network (Fig. 4).

SO_3 was lost in trace amounts (ESI Figure E5), and although the main desulfurization reaction is the degradation of aromatic rings with a simple loss of SO_2 and the formation of aromatic hydrocarbons, the sulfone compounds also form [47] as a minor by-reaction and the presence of residual sulfur can be observed by XPS (Figs. 5, 6), and some Zr-oxysulfide may also be detected by XRD (ESI Figures E6, E7, E8).

Preparation of nano-ZrO_2@C composites by high-temperature isothermal heat treatment of X-DVB-Zr samples

The 2-DVB-Zr and 8-DVB Zr samples were heated isothermally in a tube furnace between 1000 and 1400 °C. First, the swelling water content of X-DVB-8 samples released and surface melting forms ball-shaped drops, whose surface is carbonized fast due to the heat shock, even before complete liquefaction of the resin particles. The solid carbonaceous layer on the surface of the beads keeps their ball-like shape during carbonization/carbide formation [24–26].

Carbonization resulted in ZrO_2 formation due to the oxygen-rich coordination environment of zirconium. The formation of ZrO_2 (monoclinic or tetragonal), its relative amounts and the size of each ZrO_2 polymorph, and that of carbon (graphite or amorphous) prepared by carbonization of 2- and 8-DVB-Zr samples depend on temperature, DVB content and reaction time (Table 2). Prolonged heating (8 h) at 1400 °C resulted in an unknown cubic phase (a = 0.76 nm) in a minor amount. The particle size of nano-ZrO_2@C composites prepared from 2-DVB resin between 1000 and 1400 °C was smaller (~ 30–40 nm) than the size

Table 3 Surface composition (atomic %) of 8-DVB-Zr-1400–2 and 8-DVB-ZrC-(H_2) composites measured by XPS

Sample	O	C	C-O	C-OO	C-Zr	t Zr-O	Zr-O	Zr-C
8-DVB-ZrC(H2)	23.0	58.5	10.4	4.0	2.2	1.2	0.5	0.2
8-DVB-Zr-1400–2	8.8	76.0	10.8	3.3		0.8	0.3	

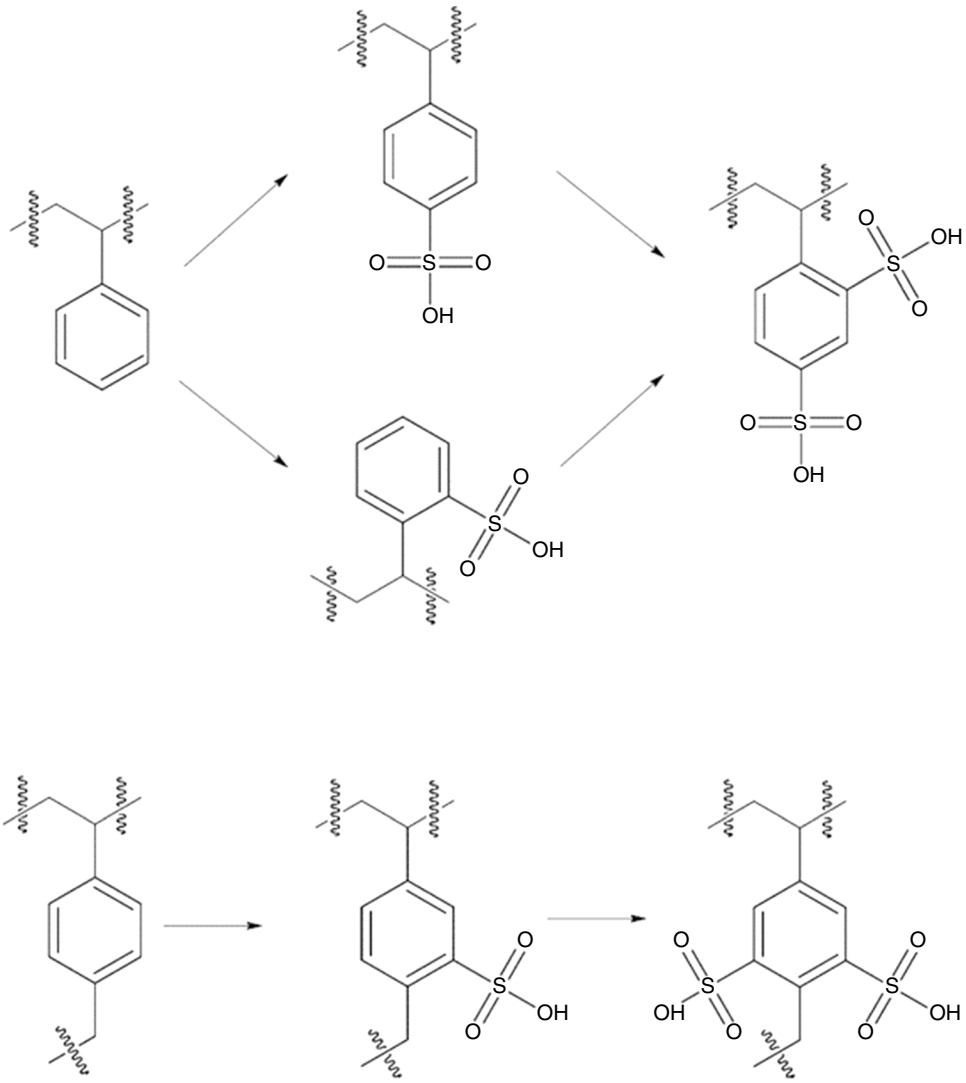

Fig. 1 Sulfonation pathways of DVB units in STY-DVB copolymers

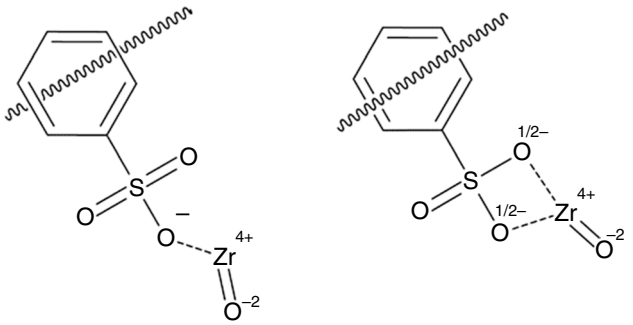

Fig. 2 Mono- and bidentate coordination mode binding of zirconyl ion to sulfonate ion

of particles prepared from 8-DVB samples (~60–70 nm) (Table 2) under the same conditions.

In all experiments, two types of carbons—graphite and amorphous carbon—were produced. Their relative amounts strongly depend on the above-mentioned conditions. In general, the amount of graphite decreases, whereas the amorphous C content increases with increasing carbonization temperature and reaction time (Table 2). Due to the low reactivity of ZrO_2 polymorphs toward carbon, no zirconium carbide formed up to 1400 °C.

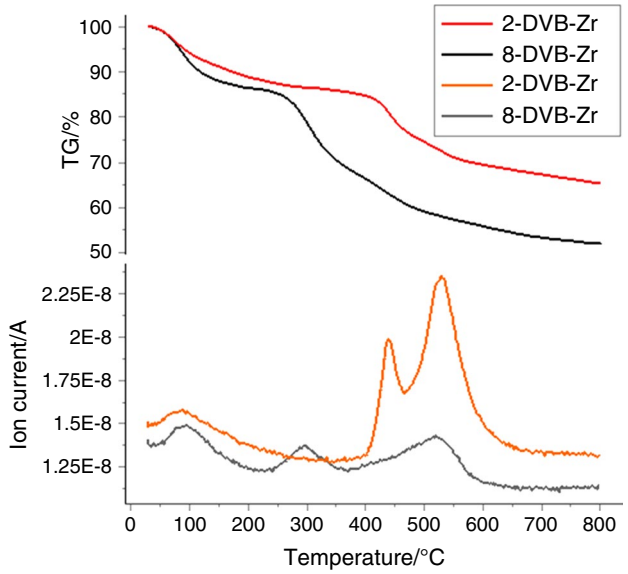

Fig. 3 TG-MS of 2-DVB-Zr and 8-DVB-Zr (m/z = 44, CO_2)

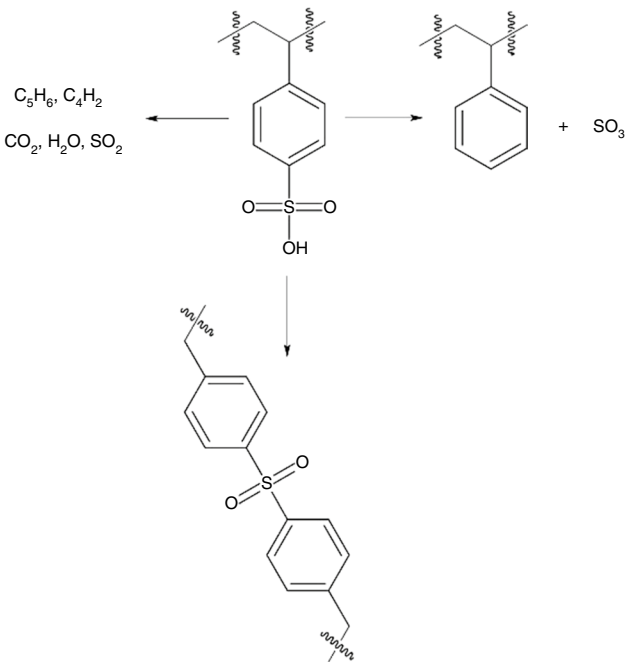

Fig. 4 Decomposition mechanism of the polymer network

Preparation and properties of nano-(ZrC, ZrO_2)@C composites in the RF plasma-assisted thermal treatment of nano-ZrO_2@C

The direct RF plasma treatment of 2- and 8-DVB-Zr samples was not successful due to their high water content and the short residence time of the injected grains in the plasma, which ultimately led to incomplete carbonization. However, RF thermal plasma treatment offers suitable conditions for the dehydrated intermediates for an in-flight reaction between ZrO_2 and carbon [22, 55]. For those tests, the 8-DVB-ZrO_2-1000–2 sample was selected and plasma processing was performed under an inert (He) and reducing atmosphere (H_2), respectively.

The RF plasma treatment of 8-DVB-ZrO_2-1000–2 resulted in the partial conversion of nano-ZrO_2 (tetragonal and monoclinic) into zirconium carbide and cubic-ZrO_2. Lattice constant calculations [54] proved that a non-stoichiometric $ZrC_{0.93}$ formed. Neither the $ZrC_{0.93}$ content nor the size of $ZrC_{0.93}$ or ZrO_2 polymorphs (11 and 13%, 23 and 21 nm ($ZrC_{0.93}$), 18–20 nm (monoclinic ZrO_2), 27–27 nm (tetragonal ZrO_2) and 22–27 nm (cubic ZrO_2)) changed significantly in the different atmospheres (He or H_2) during the plasma treatment (Table 2). The formation of a small amount of Zr_3C_2 ($ZrC_{0.67}$) was also detected (ESI Figure E8) in the H_2 atmosphere. All the amorphous carbon was transformed into graphite during the plasma treatment.

Surface characterization of the nano-ZrO_2@C and nano-(ZrC,ZrO_2)@C composites

The surface of the nano-ZrC- and nano-ZrO_2-decorated carbon (graphite) balls was characterized by physisorption method, XPS, and TEM. The BET surface area of the tube furnace-treated samples was generally below 50 $m^2\,g^{-1}$ (ESI Table E5), except for the sample 8-DVB-1400–8, whose surface area was 136 $m^2\,g^{-1}$. This increased value could probably be attributed to the presence of a cubic phase, which probably considerably contributed to the large surface area of the 8-DVB-Zr-1400–8 composite.

The surface characteristics of the nano-ZrO_2@C (8-DVB-Zr-1400–2) and nano-(ZrC, ZrO_2)@)C (H_2) composites were determined. Zirconium and carbon are present in various chemical states, as illustrated by the Zr_{3d} and C_{1s} spectra in Figs. 5 and 6. Zirconium is found in its carbide form (Zr3d5/2 179.4 eV) only in the 8-DVB-ZrC(H_2) sample (the appropriate carbon signal of ZrC is strongly covered by the signal of graphite). Zirconium is also present in oxide (Zr3d5/2 182.8 eV) form. The monoclinic, tetragonal and cubic ZrO_2 phases can be distinguished in the Zr3d spectrum. The line positions of the corresponding carbon, C1s 182.0 eV, and oxygen, O1s 531.2 eV, agree with the literature data [56]. The appearance of the ZrO_2 minor phase can be attributed to the high affinity between Zr and O [57, 58]. Part of the oxygen is chemically bound to carbon (O1s 533.0 ± 0.2 eV, C1s 286.7 ± 0.2 eV).

As can be seen from Table 3, the zirconium carbide did not form in a tube furnace, even in 2 h at 1400 °C. Only the two (monoclinic and tetragonal) polymorphs of ZrO_2 and graphite were detected on the surface of the sample. The plasma-treated 8-DVB-ZrC(H_2) sample had nearly twice

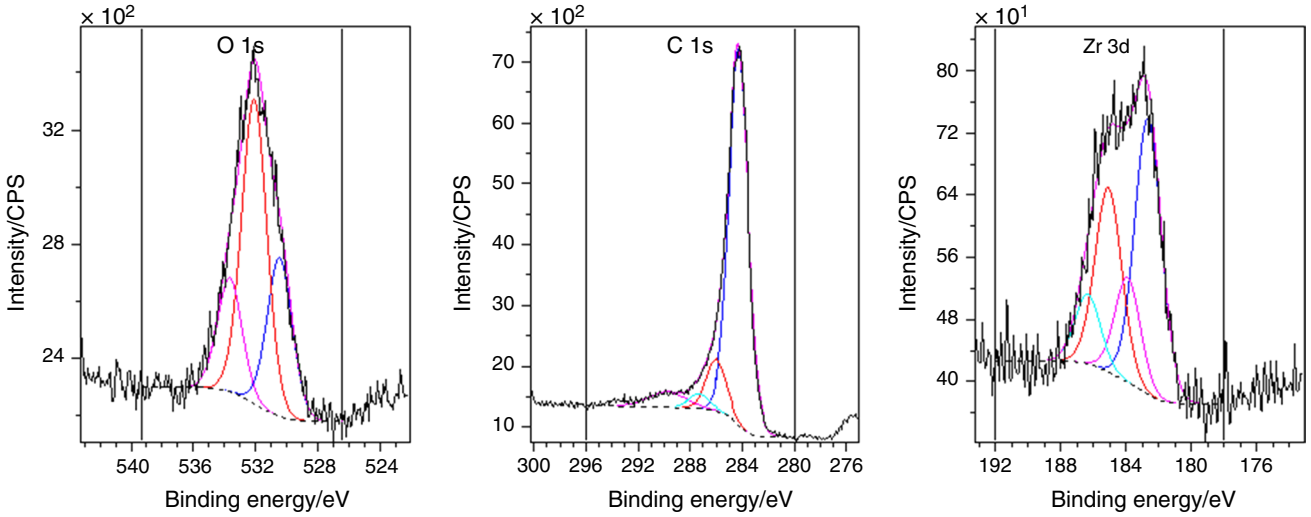

Fig. 5 X-ray photoelectron spectra of the O1s, C1s and Zr3d lines of the zirconium composite products prepared from 8-DVB-Zr-1400–8

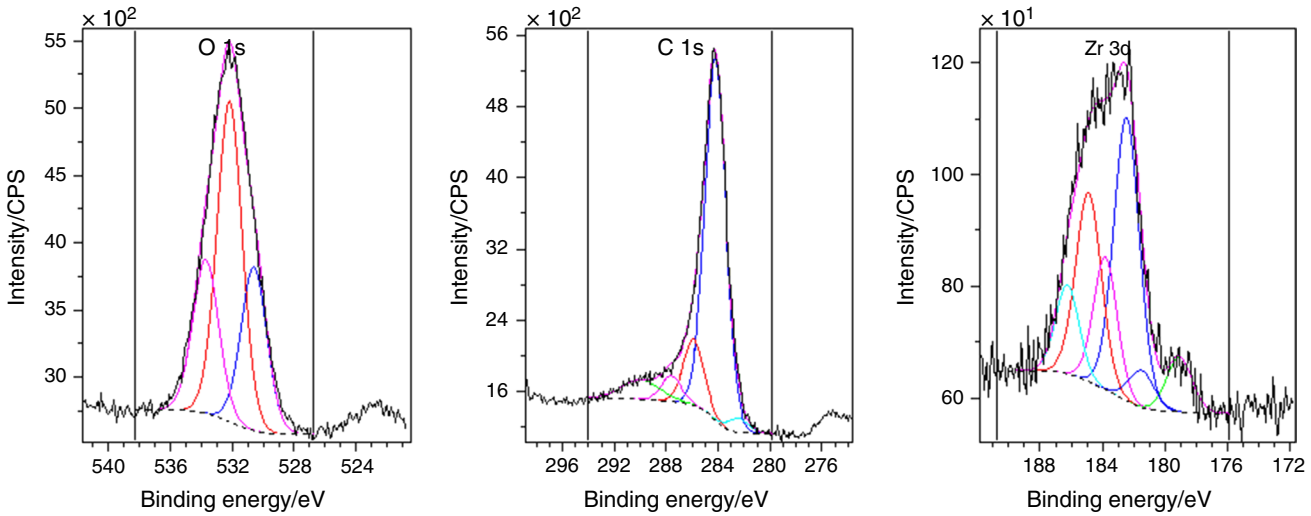

Fig. 6 X-ray photoelectron spectra of the O1s, C1s and Zr3d lines of the zirconium composite products prepared from 8-VAR-Zr-ZrC by plasma synthesis in an H_2 atmosphere

the zirconium content on its surface as the 8-DVB-1400–2 sample. Plasma treatment resulted in the formation of new surface phase: ZrC.

The carbon in both samples were partially oxidized. The two C-O components can be assigned to C–C and O-C-O bonds. The concentrations of the oxidized carbons are almost identical (Table 3).

TEM analysis of plasma-treated samples

We investigated the microstructure of 8-DVB-Zr-1400–8 and 8-DVB-ZrC (H_2) composites by TEM. In BFTEM images, the carbon matrix can be recognized by its bright contrast, whereas the particles containing Zr are dark (Fig. 7). In contrast, in HAADF images, the contrast is reversed (Fig. 8). As a result of heat and plasma treatments, the original amorphous carbon matrix became poorly crystalline graphite and both samples contained a high amount of unreacted ZrO_2 (blue arrows).

Only the plasma-treated sample contains ZrC (Fig. 7c, d), which we associate with the effective decomposition of zirconia during the plasma treatment. Although, in theory, the precursor ZrO_2 particles passing through the plasma flame should evaporate, only a small portion dissociated due to the insufficient dwell time in the hottest zone of the plasma. The appropriate residence time varied depending on both the size and the actual thermal trajectory of the individual particles.

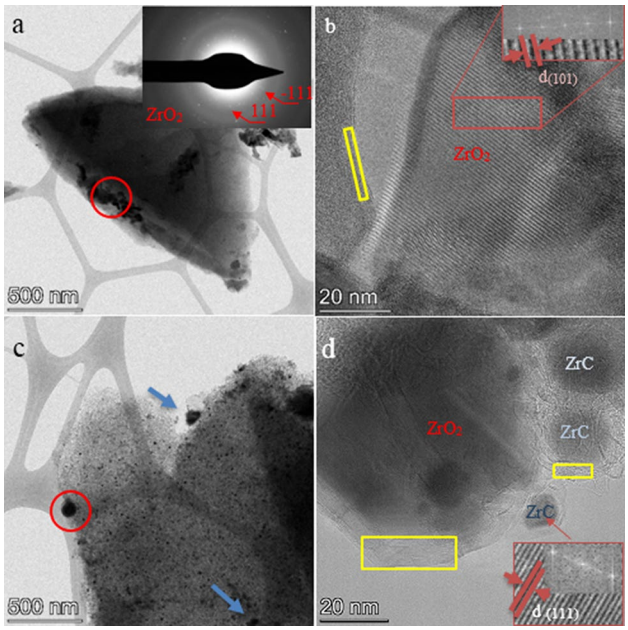

Fig. 7 TEM images of 8-DVB-Zr-1400–8 (**a**, **b**) and 8-DVB-ZrC (H_2) (**c**, **d**) samples. The characteristic (101) and (111) **d** spacings corresponding to 0.2954 nm and 0.2709 nm of ZrO_2 and ZrC are marked on insets **b** and **d**, respectively. The parts marked with yellow show graphite. (Color figure online)

The EDX composition maps (Fig. 8) suggest that the grains containing Zr are embedded in the carbon matrix. Surprisingly, the maps indicate sulfur content in all the samples. Sulfur dominantly occurs in environments containing oxygen. Thus, it is probably a TiS_xO_y-type compound (oxysulfide), whereas the sulfur content detected in the 8-DVB-ZrO_2-1400–8 sample can be associated with Zr_xS_y.

Conclusions

We have developed a simple method to prepare nano($ZrC_{0.93}$, ZrO_2 polymorph)@carbon composites with adjustable Zr/C ratio in two-step (tube furnace and plasma-assisted heat treatment) pyrolysis of zirconium-loaded sulfonated styrene(STY)-divinylbenzene(DVB) copolymers. Pre-pyrolysis of zirconium-loaded sulfonated STY-DVB ion exchangers with 2 and 8 mass % DVB at temperatures between 1000 and 1400 °C (in a tube furnace) in 2 h led to nano-ZrO_2@C with particle sizes of ~ 30–60 nm without ZrC formation. Plasma processing produced nano-($ZrC_{0.93}$, ZrO_2)@C composites with 11% (under He) (C/Zr = 73) or 13% (under H_2) (C/Zr = 58) $ZrC_{0.93}$ content. Three polymorphs of the zirconium dioxide (tetragonal, monoclinic and cubic with 18–27 nm sizes) were found in the products. The average particle size of $ZrC_{0.93}$ prepared in this way was 21–23 nm. The BET surface area of the nano-($ZrC_{0.93}$, ZrO_2)@C(graphite) composites prepared in He and H_2 was over 250 and 300 $m^2 g^{-1}$, respectively. We developed a reproducible and easy method to prepare nano-(ZrC, ZrO_2)@C products by setting the DVB content, sulfonation degree, Zr-loading and the thermal treatment conditions, which have an influence on the ZrC and graphite/amorphous carbon content of nano-ZrO_2@C intermediates.

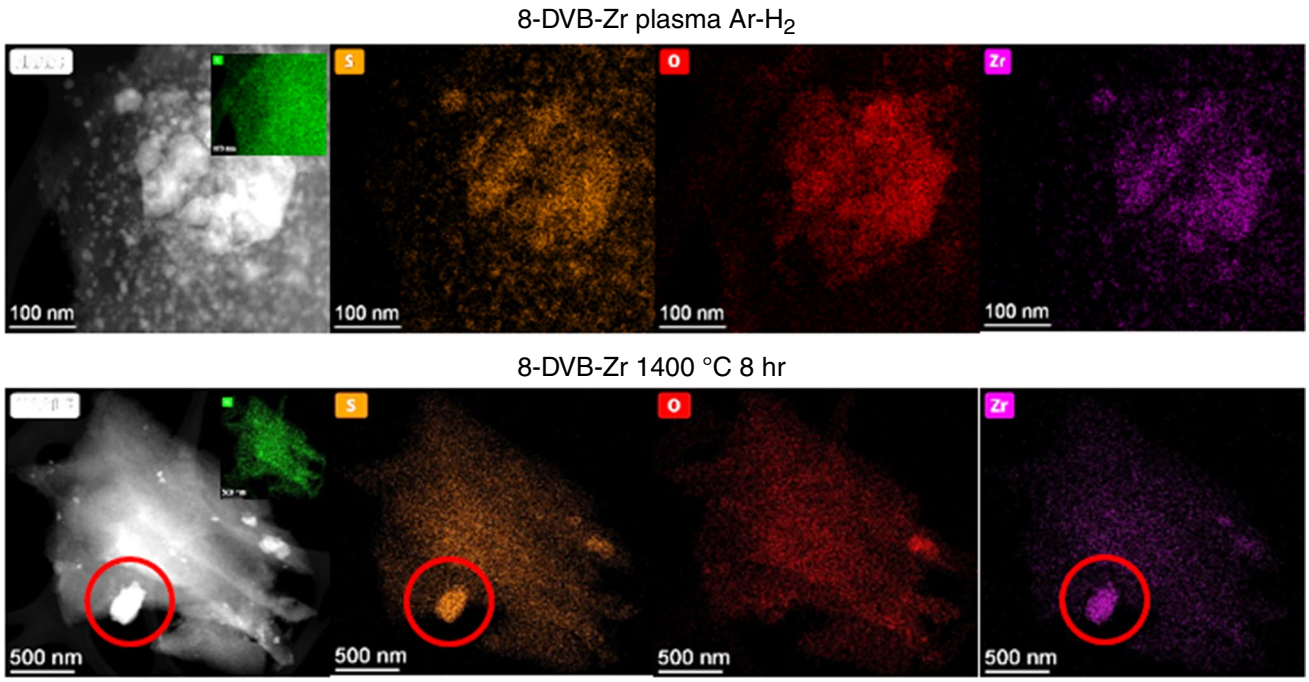

Fig. 8 HAADF images and carbon (green), sulfur (orange), oxygen (red) and zirconium. (Color figure online)

Supplementary Information The online version contains supplementary material available at https://doi.org/10.1007/s10973-022-11236-4.

Acknowledgements The research was supported by the European Union and the State of Hungary (co-financed by the European Regional Development Fund, VEKOP-2.3.2-16-2017-00013). We thank Mónika Bősze (ELTE, Chemistry Department) for elemental analysis. We are grateful to the staff and for the use of the NANOLAB facility in the University of Pannonia.

Funding Open access funding provided by ELKH Research Centre for Natural Sciences.

References

1. Liu G, Cheng L, Li K, Chen Z, Xiong X, Luan X. Damage behavior of atomic oxygen on zirconium carbide coating modified carbon/carbon composite. Ceram Int. 2020;3:3324–31.
2. Pierson HO. Handbook of refractory carbides and nitrides: properties, characteristics, processing and applications. Bergen: Noyes Publication; 1997.
3. Scales N, Chen J, Aughterson RD, Karatchevtseva I, Stopic A, Lumpkin GR, et al. Porous ZrC-carbon microspheres as potential insoluble target matrices for production of 188W/188Re. J Radioanal Nucl Chem. 2018;318(2):835–47. https://doi.org/10.1007/s10967-018-6059-y.
4. Scales N, Chen J, Hanley TL, Riley DP, Lumpkin GR, Luca V. Hierarchically porous carbon–zirconium carbide spheres as potentially reusable transmutation targets. Microporous Mesoporous Mater. 2015;212:100–9. https://doi.org/10.1016/j.micromeso.2015.03.025.
5. Dunlap CJ, Mcneff CV, Stoll D, Carr PW. Zirconia stationary phases for extreme separations. Anal Chem. 2001;73(21):599A-607A.
6. Cheng W, Campolongo MJ, Tan SJ, Luo D. Freestanding ultrathin nano-membranes via self-assembly. Nano Today. 2009;4(6):482–93.
7. Byrappa K, Ohara S, Adschiri T. Nanoparticles synthesis using supercritical fluid technology towards biomedical applications. Adv Drug Deliv Rev. 2008;60(3):299–32714.
8. Hussain I, Jalil AA, Hamid MYS, Hassan NS. Recent advances in catalytic systems in the prism of physicochemical properties to remediate toxic CO pollutants: A state-of-the-art review. Chemosphere. 2021; 277(130285).
9. Zarschler K, Rocks L, Licciardello N, Boselli L, Polo E, et al. Ultra small inorganic nanoparticles: State-of-the-art and perspectives for biomedical applications. Nanomedicine. 2016;12(6):1663–701.
10. Dou B, Wang C, Song Y, Chen H, Jiang B, Yang M, et al. Solid sorbents for in-situ CO_2 removal during sorption-enhanced steam reforming process: a review. Renew Sustain Energy Rev. 2016;53:536–46.
11. Ciddor L, Bennett JA, Hunns JA, Wilson K, Lee AF. Catalytic upgrading of bio-oils by esterification. J Chem Technol Biotechnol. 2015;90:780–95. https://doi.org/10.1002/jctb.4662.
12. Wang C, Cheng R, Liao L, Duan X. High-performance thin-film electronics based on inorganic nanostructures and composites. Nano Today. 2013;8(5):514–30.
13. Basumatary S. Transesterification with heterogeneous catalyst in production of biodiesel: A review. J Chem Pharm Res. 2013;5:1–7.
14. Fedorov PP, Yarotskaya EG. Zirconium dioxide. Review. Kondensirovannye Sredy I Mezhfaznye Granitsy = Condensed Matter and Interphases, 2021;23(2), 169–187. https://doi.org/10.17308/kcmf.2021.23/3427
15. Zhang MX, Hu QD, Huang B, Li JG. Fabrication of ZrC particles and its formation mechanism by self-propagating high-temperature synthesis from Fe–Zr–C elemental powders. J Alloy Compd. 2011;509(31):8120–5. https://doi.org/10.1016/j.jallcom.2011.05.078.
16. Alekseeva TI, Galevsky GV, Rudneva VV, Cherepanov AN, Stafetsky L, Galevsky SG. Analysis of modern production of zirconium carbide. IOP Conf Ser Mater Sci Eng. 2018;411:012006–012006. https://doi.org/10.1088/1757-899x/411/1/012006.
17. Ikawa K, Iwamoto K. Coating microspheres with zirconium carbide-carbon alloy. J Nucl Mater. 1974;52(1):128–30. https://doi.org/10.1016/0022-3115(74)90036-1.
18. Ikawa K. Vapor deposition of zirconium carbide-carbon composites by the chloride process. J Less Common Metals. 1972;29(3):233–9. https://doi.org/10.1016/0022-5088(72)90111-7.
19. Wang JX, Ni DW, Dong SM, Yang G, Gao YF, Kan YM, et al. Synthesis of nanocrystallized zirconium carbide based on an aqueous solution-derived precursor. RSC Adv. 2017;7(37):22722–7. https://doi.org/10.1039/c7ra02586f.
20. Li F, Huang X, Zhang GJ. Scalable foaming assisted synthesis of ZrC nanopowder by carbothermal reduction. Ceram Int. 2015;41:3335–8.
21. Sacks MD, Wang CA, Yang Z, Jain A. Carbothermal reduction synthesis of nanocrystalline zirconium carbide and hafnium carbide powders using solution-derived precursors. J Mat Sci. 2004;39(19):6057–66. https://doi.org/10.1023/b:jmsc.0000041702.76858.a7.
22. Martiz A, Károly Z, Bódis E, Fazekas P, Mohai M, Bertóti I, et al. In-flight synthesis of Nanosized ZrC particles from various precursors in RF-Thermal Plasma. Periodica Polytech, Chem Eng. 2021;65(3):331–42. https://doi.org/10.3311/ppch.16574.
23. Zhou Y, Heitmann TW, Bohannan E, Schaeperkoetter JC, Fahrenholtz WG, Hilmas GE. Carbon vacancy ordering in zirconium carbide powder. J Am Ceram Soc. 2020;103(4):2891–8. https://doi.org/10.1111/jace.16964.
24. Kótai L, Pasinszki T, Czégény Z, Bálint S, Sajó I, May Z, et al. Metal and metal-sulphide containing carbons from sulphonated styrene-divinylbenzene copolymer based ion-exchangers. Eur Chem Bull. 2012;1(10):398–400.
25. Pasinszki T, Krebsz M, Chand D, Kótai L, Homonnay Z, Sajó IE, et al. Carbon microspheres decorated with iron sulfide nanoparticles for mercury(II) removal from water. J Mat Sci. 2020;55:1425–35.
26. Pasinszki T, Krebsz M, Kótai L, Sajó IE, Homonnay Z, Kuzmann E, et al. Nanofurry magnetic carbon microspheres for separation processes and catalysis: synthesis, phase composition, and properties. J Mater Sci. 2015;50(22):7353–63. https://doi.org/10.1007/s10853-015-9292-6.

27. Shigeharu N, Shinichi, H. Preparation of carbon products. JPS57191213 (A), C01B31/02. 1981.
28. Fazekas P, Bódis E, Keszler AM, Czégény Z, Klébert S, Károly Z, et al. Decomposition of Chlorobenzene by thermal plasma processing. Plasma Chem Plasma Process. 2013;33(4):765–78. https://doi.org/10.1007/s11090-013-9459-3.
29. Fazekas P, Czégény Z, Mink J, Bódis E, Klébert S, Németh C, et al. Decomposition of poly(vinyl chloride) in inductively coupled radiofrequency thermal plasma. Chem Eng J. 2016;302:163–71. https://doi.org/10.1016/j.cej.2016.05.044.
30. Solt HE, Németh P, Mohai M, Sajó IE, Klébert SZ, Franguelli FP, Fogaca L, Pawar R, Kótai L. Synthesis of copper manganites along the borderline of the amorphous/crystalline state and their catalytic activity. ACS Omega. 2021;6:1523–33.
31. Trif L, Franguelli FP, Lendvay G, Majzik E, Béres K, Bereczki L, et al. Thermal analysis of solvatomorphic decakis(dimethylammonium) dihydrododecatungstate. J Therm Anal Calorim. 2021;144:81–90.
32. Béres KA, Petruševsk V, Holló BB, Német P, Fogaca L, Franguelli FP, et al. $AgNO_3$ NH_4NO_3 - an enigmatic double-salt type "decomposition intermediate" of diamminesilver(I) permanganate. Zeitschrift für Anorganische und Allgemenien Chemie. 2021;647(11):1166–74.
33. Fogaça LA, Bereczki L, Petrusevski VM, Barta-Holló B, Franguelli FP, Mohai M, et al. A Quasi-intramolecular solid-phase redox reaction of ammonia ligands and perchlorate anion in Diamminesilver(I) Perchlorate. 2021; https://doi.org/10.3390/inorganics9050038.
34. Fogaca LA, Kováts E, Németh G, Kamarás K, Béres KA, Németh P, et al. Solid-phase quasi-intramolecular redox reaction of 2 $[Ag(NH_3)_2]MnO_4$: an easy way to prepare pure $AgMnO_2$. Inorg Chem. 2021;60(6):3749–60.
35. Evans S, Pritchard RG, Thomas JM. Relative differential subshell photoionisation crosssections (MgKα) from lithium to uranium. J Electron Spectr Related Phenomena. 1978;14:341–58.
36. Reilman RF, Msezane A, Manson ST. Relative intensities in photoelectron spectroscopy of atoms and molecules. J Electron Spectr Related Phenomena. 1976;8:389–94.
37. Pechishcheva NV, Shunyaev KY, Melchakova OV. Zirconium in modern analytical chemistry. Rev Anal Chem. 2018. https://doi.org/10.1515/revac-2017-0016.
38. Devia DH, Sykes AG. Aqueous solution chemistry of zirconium(IV). 1. Kinetic studies on hydrogen ion and general acid (HX) induced dissociations of the tetrameric ion [Zr4(OH)8(H2O)16]8+. Inorg Chem. 1981;20(3):910–3. https://doi.org/10.1021/ic50217a054.
39. Lokshin EP, Tareeva OA. Sorption of zirconium from nitrate and sulfate solutions. Theor Found Chem Eng. 2019;53(4):688–92. https://doi.org/10.1134/s0040579519040122.
40. Clearfield A. Structural aspects of zirconium chemistry. Rev Pure Appl Chem. 1964;14:91–108.
41. Fathy M, Moghny TA, Awadallah AE, El-Bellihi AHAA. Nano composites of polystyrene divinylbenzene resin based on oxidized multi-walled carbon nanotubes. Int J Mod Org Chem. 2013;2(1):67–80.
42. Shishlov NM, Khursan SL. Effect of ion interactions on the IR spectrum of benzenesulfonate ion. Restoration of sulfonate ion symmetry in sodium benzenesulfonate dimer. JMol Struct. 2016;1123:360–6. https://doi.org/10.1016/j.molstruc.2016.06.030.
43. De R, Lee H, Das B. Exploring the interactions in binary mixtures of polyelectrolytes: Influence of mixture composition, concentration, and temperature on counterion condensation. J Mol Liq. 2018;251:94–9.
44. Detoni S, Hadzi D. Infra-red spectra of some organic sulphur-oxygen compounds. Spectrochim Acta. 1956;11:601–8. https://doi.org/10.1016/s0371-1951(56)80102-1.
45. Yuchi A, Yoshida N. Adsorption of tetravalent metal ions to chelating resins containing iminodicaceic acid groups. Bull Chem Soc Jpn. 2000;73:1841–2.
46. Byun HS, Burford RP, Fane AG. Sulfonation of crosslinked asymmetric membranes based on polystyrene and divinylbenzene. J Appl Polym Sci. 1994;52(6):825–35. https://doi.org/10.1002/app.1994.070520612.
47. Dobson KD, McQuillan AJ. An Infrared spectroscopic study of carbonate adsorption to zirconium dioxide sol gel films from aqueous solutions. Langmuir. 1997;13(13):3392–6.
48. Jiang J, May I, Sarsfield MJ, Ogden M, Fox DO, Jones CJ, et al. A spectroscopic study of the dissolution of cesium phosphomolybdate and zirconium molybdate by ammonium carbamate. J Sol Chem. 2005;34(4):443–68.
49. Fitzgerald JJ, Weiss RA. Cation-Anion and Cation-Cation interactions in sulfonated polystyrene ionomers spectroscopic studies of the effects of solvents. ACS. 1986:35–35.
50. Busca G, Lorenzelli V. Infrared spectroscopic identification of species arising from reactive adsorption of carbon oxides on metal oxide surfaces. Mat Chem. 1982;7(1):89–126. https://doi.org/10.1016/0390-6035(82)90059-1.
51. Kocsis T, May Z, Czégény Z, Sreedhar B, Pawar RP, Kótai L. Perspectives of magnetic and nanosized metal-containing amorphous carbon composite chemosorbents and catalysts. Nano Stud. 2016;14:7–35.
52. Yatsevskaya VS, Sycheva MI, A O. Properties of activated carbon produced from spent ion-exchange resins. Doklady Akademii Nauk BSSR. 1985;29(11):1010–1023.
53. Komarov VS, Yatsevskaya MI, Sycheva OA. Properties of activated carbon produced from spent ion-exchange resins. Doklady Akademii Nauk BSSR. 1985;29(11):1010–23.
54. Chinthaka Silva GW, Kercher AA, Hunn JD, Martin RC, Jellison GE, Meyer HM. Characterization of zirconium carbides using electron microscopy, optical anisotropy, Auger depth profiles, X-ray diffraction, and electron density calculated by charge flipping method. J Solid State Chem. 2012;194:91–9. https://doi.org/10.1016/j.jssc.2012.04.047.
55. Károly Z, Mohai I, Klébert S, Keszler A, Sajó IE, Szépvölgyi J. Synthesis of SiC powder by RF plasma technique. Powder Technol. 2011;214(3):300–5. https://doi.org/10.1016/j.powtec.2011.08.027.
56. Wagner C, Riggs WM, Davis LE, Moulder JF, Muilenberg GE. Handbook of X-ray Photoelectron Spectroscopy. Eden Prairie: Perkin-Elmer Corporation; 1979.
57. Chase MW, Jr. "NIST-JANAF Themochemical Tables", Journal of Physical and Chemical Reference Data, Monograph 9, NIST National Institute of Standards and Technology.1998. https://webbook.nist.gov/cgi/cbook.cgi?Source=1998CHA1-1951&Units=
58. Calderon VS, Cavaleiro A, Carvalho S. Chemical and structural characterization of Zr-C-N-Ag coatings: XPS, XRD and Raman spectroscopy. Appl Surf Sci. 2015;346:240–7. https://doi.org/10.1016/j.apsusc.2015.03.16.